01 Jan 2023

# In Situ and Real-Time Mold Flux Analysis using a High-Temperature Fiber-Optic Raman Sensor for Steel Manufacturing Applications

Bohong Zhang

Hanok Tekle

Ronald J. O'Malley
*Missouri University of Science and Technology*, omalleyr@mst.edu

Todd Sander

*et. al. For a complete list of authors, see* https://scholarsmine.mst.edu/matsci_eng_facwork/2918

### Recommended Citation

# *In Situ* and Real-Time Mold Flux Analysis Using a High-Temperature Fiber-Optic Raman Sensor for Steel Manufacturing Applications

Bohong Zhang, Hanok Tekle, Ronald J. O'Malley, Todd Sander, Jeffrey D. Smith, Rex E. Gerald II, Jie Huang, *Senior Member, IEEE*

*Abstract*—**Continuous casting in steel production uses specially developed oxyfluoride glasses (mold fluxes) to lubricate a mold and control the solidification of the steel in the mold. The composition of the flux impacts properties, including basicity, viscosity, and crystallization rate, all of which affect the stability of the casting process and the quality of the solidified steel. However, mold fluxes interact with steel during the casting process, resulting in flux chemistry changes that must be considered in the flux design. Currently, the chemical composition of mold flux must be determined by extracting flux samples from the mold during casting and then processing these samples offline to estimate the working chemical composition and, therefore, the expected properties of the flux. Raman spectroscopy offers an alternative method for performing flux analysis with the potential to perform measurements online during the casting process. Raman spectroscopy uniquely identifies specific chemical bonds and symmetries in the glassy flux by revealing peaks that are a fingerprint of the vibration modes of molecules in the flux. The intensities of specific peaks in Raman spectra can be correlated with the chemical composition of the melt and associated properties such as basicity and viscosity. This paper reports on the first use of a portable fiber-optic Raman sensor for *in situ* Raman spectroscopic measurements of molten flux at 1400 °C. The work demonstrates the advantages of fiber-optic Raman spectroscopy to document the structure and chemical composition of flux samples at temperatures typically encountered in the mold during continuous caster operation. Experimental results demonstrate that the composition-dependent Raman signal shifts can be detected at caster operating temperatures, and the use of high-temperature Raman analysis for in-line flux monitoring shows significant promise for the *in situ* detection of changes in flux composition and physical properties during casting.**

*Index Terms*—**In situ fiber-optic Raman sensor; High-temperature Raman spectroscopy; Mold flux; Basicity; Viscosity; oxyfluoride glasses; Composite material; Steel manufacturing.**

## I. INTRODUCTION

In recent years, there have been numerous studies on the effects of mold flux compositions on continuous cast steel quality.

Mold fluxes used to produce advanced high-strength steels have received considerable attention due to the enhanced strength and formability associated with these steels [1], [2]. In addition, advanced high-strength steels are often designed with a high aluminum content, which improves the mechanical properties of the steel and potentially makes the steel product lighter in weight. However, aluminum in steel can also react with $SiO_2$ in the flux through an exchange reaction that diminish the amount of $SiO_2$ from the flux and drives $Al_2O_3$ into the flux, causing significant changes in the in-service flux chemistry and steel properties [3]-[5]. During casting, changes in the mold flux properties can result in catastrophic adhesion of the solidified steel shell to the mold (sticking) due to reduced or interrupted mold lubrication or changes in mold heat removal, which negatively impact shell growth in the mold. Therefore, it is essential to study the effects of in-service flux chemistry changes on the casting process.

Mold fluxes used for casting high-aluminum steels are generally based on $CaO$-$Al_2O_3$-$SiO_2$-containing oxyfluoride glasses [6]-[8] and are either designed with low $SiO_2$ content (high basicity) to suppress the reaction or with high $SiO_2$ content (low basicity) to tolerate the $SiO_2$ loss in service. The changes in viscosity of these mold fluxes have been investigated in situations where $Al_2O_3$ gradually replaces $SiO_2$ [5], [9]. Viscosity was observed to increase as $SiO_2$ replaced $Al_2O_3$. The flux crystallization temperature also increased as the $SiO_2$ content of the flux decreased, and basicity increased. Both conditions result in the degradation of the flux lubricating properties in the mold [10]. The effect of $Na_2O$ and $Li_2O$ additions on the viscosity and crystallization rate of these fluxes has also been investigated [6], [11]. These additions reduce the viscosity of the flux by donating oxygen anions that break the chains in the silicate network. On cooling, cuspidine ($Ca_4Si_2O_7F_2$) is often reported as the main crystalline phase in these fluxes [8]. The size of cuspidine increases, while the number of cuspidine decreases with increasing mold flux basicity. Additionally, other research has reported a strong

Bohong Zhang, Rex E. Gerald II, and Jie Huang are with the Department of Electrical and Computer Engineering, Missouri University of Science and Technology, Rolla, MO 65409 USA (e-mail: jieh@mst.edu).

Hanok Tekle, Ronald J. O'Malley, Todd Sander, and Jeffrey D. Smith are with the Department of Material Science and Engineering, Missouri University of Science and Technology, Rolla, MO 65409 USA.

crystallization tendency and changes in crystallite phases with changes in flux chemistry, highlighting the complex nature of these flux materials and the subsequent consequences to modern steel-making processes and long steel products [12].

In addition to the influences of flux compositions on the quality of long steel products, the viscosity and crystallization behavior of the mold flux are two of the most critical factors in continuous casting that affect the casting process. The flux basicity and viscosity significantly impact both the absorption of inclusions [40] and the corrosion of the submerged entry nozzle (SEN) in the mold. Most importantly, optimizing the molten flux basicity and viscosity can inhibit mold sticker events by providing optimal lubrication at the mold interface. Overall, optimized fluxes benefit continuous casting operations. Therefore, basicity and viscosity must be controlled during the mold flux design [13]-[15] and throughout caster operation. Furthermore, the crystallization behaviors and viscosities of mold fluxes were strongly influenced by the molecular structures that comprised glassy fluxes, and changes in composition affect both the viscosity [12], [16]-[18] and crystallization behavior [12], [16], [17]. Since mold flux is a multi-component slag system, it usually contains more than five components. In addition, these fluxes have a complex structure that changes during contact with surfaces (e.g., steel, refractories), so controlling the basicity and viscosity of the flux becomes more difficult. Therefore, a method that allows the structure and viscosity of mold fluxes to be studied and adjusted in real-time at high temperatures could have transformative implications for the steel manufacturing industry.

Raman spectroscopy can identify the presence of molecules non-destructively through their unique Raman fingerprint (vibration bands) [19]-[22]. This optical spectroscopic technique has been fully developed and applied in many practical applications, such as cement chemistry, to study hydration and deterioration [23], [24]. Moreover, it has a significant advantage over other techniques in distinguishing $H^+/OH^-$, liquid/solid water molecules, and metallic elements (Fe and Al) [25]-[27]. Advances in the development of optical fibers for telecommunication have led to the use of optical fibers for the design of *in situ* Raman probes for biomedical applications [28]-[30]. Furthermore, besides applications in chemistry, civil construction, and medicine, other scientific researchers have presented preliminary studies applying Raman spectroscopy at extremely high temperatures to study the chemical property of molten materials [31]-[33]. For example, several studies of using high-temperature Raman spectroscopy were reported to investigate the aluminosilicate liquids and $SiO_2$ glass liquids [31], [33]. The investigators performed preliminary studies of high-temperature Raman spectroscopy using a miniature electric wire heating device and bench top Raman system. The results demonstrated correlations between high-temperature Raman spectra and chemical structures in the liquid, which contributed to an understanding of the molten sample's chemical properties. However, the miniature electric heating device employed a 0.5 - 0.8 mm diameter heated wire loop to hold the glass sample, which dramatically limits the volume and size of the test sample. Secondly, the lack of portability of the benchtop Raman system also limits the application of high-temperature Raman techniques to practical industrial and production applications. What is needed is a probe head that can be positioned proximate to a high-temperature molten material, remote from the Raman spectrometer. Optical fibers made of glass or sapphire can withstand very high temperatures and are efficient conduits of photons over long distances.

This paper introduces, for the first time, a portable remote fiber-optic Raman sensor that can be used for *in situ* real-time measurements of materials at high temperatures. In previous experimental studies, microscopic Raman spectroscopy of melted and rapidly quenched samples investigated the effects of $SiO_2$, CaO, and $Al_2O_3$ on the distribution of silicate anion species in calcium silicate systems. Specific peaks in Raman spectra were correlated with flux chemistries and viscosity values [12], [16], [17]. The work reported here aims to use a remote fiber-optic probe head to record Raman spectroscopy at 1400 °C to evaluate the real-time structure and chemical composition of mold flux samples. The experimental results show that composition-dependent Raman signals can be detected at high temperatures and that online flux analysis using a high-temperature Raman system shows excellent promise. A deconvolution algorithm was applied to deconvolute peaks from the original Raman spectrum. Ratios of judiciously selected the Raman peak intensities and areas were compared and correlated with the chemical composition and physical material properties. The relationships between the structure and the thermo-physical properties of silicate melts, such as basicity, viscosity, and density, were evaluated. Strong correlations were observed both from tests performed with synthetic flux samples and with complex industrial flux samples. Until now, fiber-optic Raman techniques have not been applied to the steel industry to study the chemical structure of fluxes and slags under high-temperature conditions, *in situ*. The ability to remotely control molten flux compositions through *in situ* chemical fingerprinting using real-time Raman signal analyses could significantly impact the in line slag and flux composition analysis and continuous casting in the steel industry.

## II. EXPERIMENTAL

### A. Materials and Sample Preparation

To investigate the substitutional and combined effects of composition on the structure of a mold flux at 1673K (1400 °C) via Raman spectroscopy, a series of synthetic mold fluxes was fabricated based on typical constituents of a $CaO-Al_2O_3-SiO_2$ oxyfluoride mold flux. Previous studies have noted that viscosity can be adjusted by changing the $CaO/SiO_2$ ratio [16]-[18]. Another effect of the $CaO/SiO_2$ ratio on the mold flux structure is the coordination behavior of alumina. When $Al_2O_3$ is introduced into the silicate network, the $Al^{3+}$ ions can be absorbed into the silicate structure, acting as the network formers and breakers [12], [34], depending on basicity. Therefore, mold flux that contains $Al_2O_3$ increases the complexity of the silicate structure and exhibits the properties

change of mold flux. In the four synthetic flux samples studied in this work, the $Al_2O_3$ content was fixed at 4.69 wt% by varying the $SiO_2$ and CaO content to control the basicity value for the samples. Table I. shows four synthetic flux samples, S1 through S4, with the calculated basicity values (VB=$CaO/SiO_2$) of 0.84, 0.99, 1.15, and 1.3. The samples were prepared from reagent-grade chemicals, $SiO_2$, CaO, $Al_2O_3$, $Na_2O$, and fluoride.

TABLE I. THE CHEMICAL COMPOSITION (IN %) OF FOUR SYNTHETIC FLUX SAMPLES USED IN THIS STUDY.

|  | $SiO_2$ | CaO | $Al_2O_3$ | $Na_2O$ | Fluoride | VB |
|---|---|---|---|---|---|---|
| S1 | 42.87 | 35.87 | 4.69 | 7.5 | 9.07 | 0.84 |
| S2 | 39.49 | 39.24 | 4.69 | 7.5 | 9.07 | 0.99 |
| S3 | 36.61 | 42.15 | 4.69 | 7.5 | 9.07 | 1.15 |
| S4 | 34.11 | 44.63 | 4.69 | 7.5 | 9.07 | 1.3 |

### B. Fiber-Optic Raman System

A high-temperature fiber-optic Raman probe system was developed and employed to study the chemistry of mold fluxes in high-temperature environments. The fiber-optic Raman probe (Inphotonics, RPP532/11-5C) was constructed with a probe body and a removable extension. A 25 cm length extension probe and a 0.9 cm diameter tip are suitable for testing in the confined spaces and harsh environments associated with steel manufacturing. Inside the Raman probe, a 105 µm core diameter multimode optical fiber and a 100 µm core diameter multimode optical fiber were included for light excitation and collection, respectively. A long-pass filter and a bandpass filter (centered at 532 nm) were installed inside the probe body to block the laser reflection and eliminate the inelastic background signal generated from the optical fiber. A convex sapphire window was employed at the tip of the extension probe, providing the Raman probe an 8 mm working distance. All the fiber-optic components are encased in an outer protective jacket of 316 stainless steel affording a maximum service temperature of 650 °C.
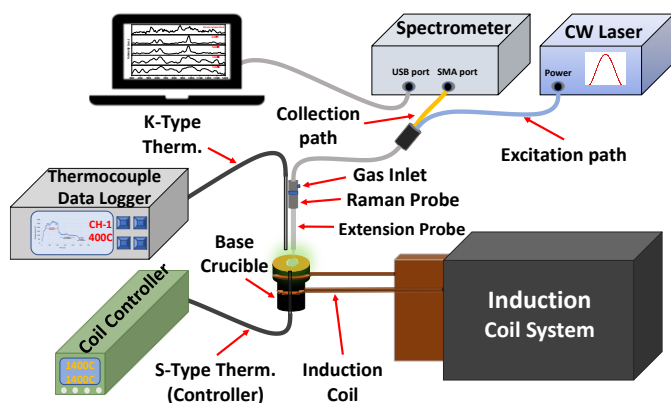


Fig. 1. Schematic diagram of the fiber-optic Raman system combined with an induction coil system for *in situ* high-temperature experiments. The working distance of the probe head to the molten flux was set to 0.8 cm to collect the highest Raman signal. The extension system, composed of optical fibers, that allows the spectrometer to operate at a safe distance from the high-temperature environment near the probe.

A series of trial experiments comparing different laser wavelengths (532 nm, 633 nm, and 785 nm) showed that the 532 nm laser did not generate strong background fluorescence when exciting the flux sample. In addition, based on Raman theory, the Raman scattering intensity is proportional to $\lambda^{-4}$, where $\lambda$ represents the laser wavelength. The 532 nm laser provided the highest Raman scattering intensity, which was best suited for this study. As shown in Fig. 1, a 532 nm laser (green laser) was used as the excitation source, and a QE-Pro spectrometer was employed to record Raman spectra with a spectral resolution of 3 $cm^{-1}$.

### C. Induction Coil Furnace Setup for High-Temperature Experiments

An induction furnace was employed to perform high-temperature Raman experiments. As shown in Fig. 1 and Fig. 2, two thermocouples (K-Type and S-Type) were installed to monitor the temperature from two different locations. The K-Type thermocouple was aligned with the tip of the Raman probe to monitor the surrounding temperature to ensure that the probe head was not overheated. The real-time temperature data was collected through a thermocouple data logger. The S-Type thermocouple was placed directly in contact with the graphite crucible that contained the molten flux sample to monitor the flux temperature. The size of the crucible was about 10 mm in diameter and 20 mm deep, and the flux sample typically formed a 10 mm diameter sphere upon melting. Using this heating system, the synthetic mold flux samples were melted and heated to 1400 °C, and high-temperature Raman spectra were collected in real-time.
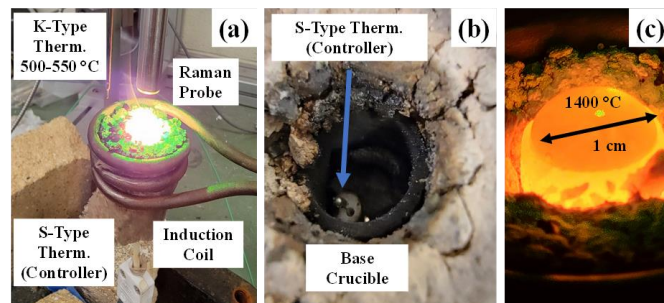


Fig. 2. Images of the *in situ* fiber-optic Raman probe in high-temperature experiment. (a) The fiber-optic Raman probe head was configured parallel to the K-type thermocouple in the experiment set-up. The K-type thermocouple monitored the temperature proximate to the probe head to protect the probe from overheating. The induction coil surrounded the crucible, which contained molten flux samples. (b)The S-type thermocouple was configured directly in contact with the base of the crucible and used to control the crucible temperature. (c) Mold flux at 1400 °C contained in a 1 cm diameter crucible.

## III. RESULTS AND DISCUSSION

### A. High-temperature Raman Spectroscopic Analysis of Synthetic Flux Samples

Considering the possible deleterious effects of natural light on the Raman signal, all high-temperature Raman signal collection was performed under dark room conditions to improve the signal-to-noise ratio. In addition, thermal radiation generated at high temperatures is a significant component of the Raman signal [31], [33]. A background subtraction method was

applied to remove the thermal radiation signal to minimize its interference with the natural Raman spectrum of the flux sample. When the furnace was heated to 1400 °C, the Raman probe was moved above the graphite crucible to collect the background light signal in a high-temperature environment. After the acquisition of the background spectrum, mold flux material was added to the graphite crucible and fully melted at 1400 °C, and the Raman spectrum was collected again. The background removal method effectively subtracted the thermal radiation signal feature from the acquired spectrum, leaving only the actual Raman signal emanated from the sample. The Raman signal integration time was set from 2 to 5 seconds for data collection. Five spectra for each measurement condition were collected and averaged to improve the signal-to-noise ratio. Four flux samples were prepared with differing compositions, as shown in Table I. The melt structures of samples 1 to 4 were then analyzed by Raman spectroscopy. The real-time Raman spectroscopy results at 1400 °C are included in Fig. 3. The Raman peaks located at 480-560 $cm^{-1}$ and 590-740 $cm^{-1}$ correspond to Al-O-Al and Si-O-Si bending vibrations, respectively. The Raman peaks located at 800-1200 $cm^{-1}$ are associated with Q(Si) bond stretching [1], [5], [9], [12], [14], [35], [36].

sample than for the S1 sample, indicating that the $SiO_2$ content has decreased. Identifying a correlation between Raman spectroscopy and chemical composition is necessary to further understand the relationship between Raman spectroscopy and flux properties. To more accurately quantify the resulting Raman spectra, a typical deconvolution method was performed on the peaks in the alumina and silica regions using Origin software. Gaussian functions were employed in the curve fitting by the deconvolution algorithm. Based on previous studies, deconvolution was performed in the intervals 480-560 $cm^{-1}$ and 590-740 $cm^{-1}$, respectively [1], [5], [9], [12], [14], [33], [35], [36]. As noted, a dual peak was captured in the 480-560 $cm^{-1}$ alumina region from the synthetic flux samples. Therefore, a hypothesis is inferred that the bridging oxygen bond in the silicate structure breaks and reacts with alumina to form another Al-O-Al chemotactic structure during the melting process. According to the previous investigation of the Al-O-Al and Si-O-Si bond [1], [5], [9], [12], the results of the deconvolution process are shown in Fig. 4. Peaks at 525 $cm^{-1}$ and 645 $cm^{-1}$ were identified as the central peaks after deconvolution. The red and green curves in the figure, corresponding to alumina and silica, respectively, are illustrated in the deconvolution results. The sum of the fitted peaks in the figure is compared with the original spectral data, and an overall fit of greater than a 96% R-squared value was achieved.
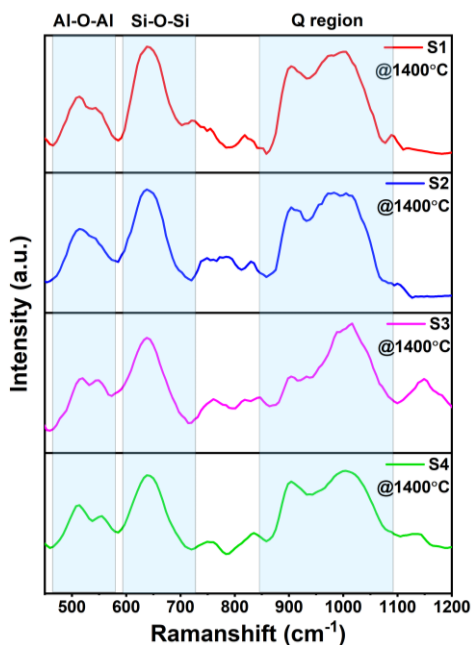


Fig. 3. Raman region from 400 to 1200 $cm^{-1}$ displaying the Raman spectra of four synthetic flux samples from S1 to S4 at 1400 °C. The spectra include the regions that provide information about alumina (480-560 $cm^{-1}$), silica (590-740 $cm^{-1}$), and the Q region (850-1100 $cm^{-1}$).
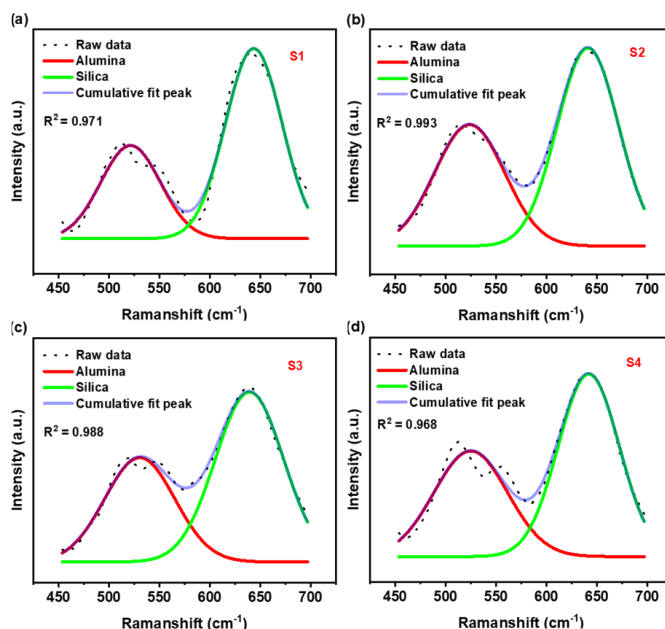


Fig. 4. Deconvoluted Raman spectra of 1400 °C synthetic fluxes for the alumina and silica regions for sample 1 to sample 4. The red and green peaks at 525 $cm^{-1}$ and 645 $cm^{-1}$ corresponded to alumina and silica.

The peak features in the Q region of four synthetic flux samples recorded at 1400 °C vary with the chemical composition of the mold flux, as shown in Fig. 3. Importantly, Al-O-Al bond stretching vibrations and the Si-O-Si bending vibration characterized by peaks at 480-560 $cm^{-1}$ and 590-740 $cm^{-1}$, respectively show no significant shifts or changes in composition. However, a preliminary comparison of the silica peak intensity of sample 1 and sample 4 reveal that the characteristic peak of silica at 645 $cm^{-1}$ is weaker for the S4

The main constituents of the synthetic mold flux are $SiO_2$, CaO, and $Al_2O_3$. The $Al_2O_3$ was fixed at 4.69 wt% in all four samples, so any structural changes are strongly affected by the $CaO/Al_2O_3$ and $SiO_2/Al_2O_3$ ratios. A quantitative comparison using absolute peak intensities of the Raman spectra for different samples is challenging. For example, unavoidable temperature fluctuation at high temperatures directly affects the background light in the Raman spectrum, and therefore, the

peak intensity. However, energy from the background light influences the entire Raman spectrum uniformly. Therefore, considering the intensity ratio of the characteristic peaks in the Raman spectra for the samples should provide a means for accurate quantifications of Raman spectra result. Completing analysis of the high-temperature Raman data then involves collecting the raw and deconvoluted Raman peaks representing Al-O-Al at 525 cm$^{-1}$ and Si-O-Si at 645 cm$^{-1}$ to establish a relative Raman ratio of peak intensities that could be compared with the chemical content ratio. The relative Raman peak intensity ratios of SiO$_2$/Al$_2$O$_3$ contents were compared with the SiO$_2$/Al$_2$O$_3$ content ratios, as shown in Fig. 5.
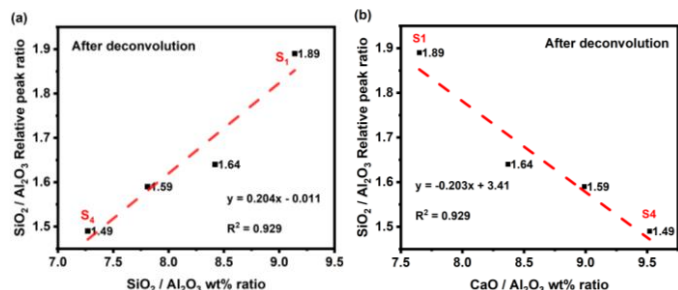


Fig. 5. Correlation of SiO$_2$/Al$_2$O$_3$ Raman peak ratio and the content ratio of SiO$_2$/Al$_2$O$_3$ and CaO/Al$_2$O$_3$. (a) demonstrates the correlation result of SiO$_2$/Al2O$_3$ to the corresponding Raman peak ratio and the content ratio of SiO$_2$/Al2O$_3$ from the deconvolution data. (b) demonstrates the correlation result of SiO$_2$/Al$_2$O$_3$ to the corresponding Raman peak ratio and the content ratio of CaO/Al$_2$O$_3$ from the deconvolution data.

The relative Raman peak intensity ratio has been compared with the chemical content ratio of SiO$_2$/Al$_2$O$_3$ for the peak intensity data extracted after deconvolution. According to the data tabulated in Table I, sample S1 has the highest amount of SiO$_2$ and the lowest amount of CaO. In contrast, sample S4 has the lowest amount of SiO$_2$ and the highest amount of CaO. According to the results shown in Fig. 5(a), sample S1, which contains the highest amount of SiO$_2$, has the highest value of the SiO$_2$/Al$_2$O$_3$ content ratio and the highest Raman peak intensity ratio. Sample S4 has the lowest amount of SiO$_2$, corresponding to the lowest value of the SiO$_2$/Al$_2$O$_3$ content ratio and the lowest Raman peak intensity ratio. The Raman peak intensity ratio of SiO$_2$/Al$_2$O$_3$ correlates positively with the chemical content ratio of SiO$_2$/Al$_2$O$_3$. Furthermore, a fitted R-squared value was calculated above 92%. Next, the Raman peak intensity ratio was analyzed with the chemical content ratio of CaO/Al$_2$O$_3$. Sample S4 contains the highest amount of CaO and the lowest amount of SiO$_2$, which has the highest content ratio of CaO/Al$_2$O$_3$, but the lowest Raman peak intensity ratio of SiO$_2$/Al$_2$O$_3$ in all four flux samples, as shown in Fig. 5(b). The SiO$_2$/Al$_2$O$_3$ Raman relative peak intensity ratio increased by increasing the SiO$_2$/Al$_2$O$_3$ content ratio. However, the content ratio of CaO/Al$_2$O$_3$ decreased, which indicates that the Raman spectra of silica and alumina from the flux samples will be affected by the degree of polymerization of the silicate and calcium oxide network. Moreover, the fiber-optic Raman system and deconvolution algorithm can be trusted for further data analysis based on the high R-squared values reported here. This data analysis shows that the correlation of the material

composition can be obtained using the deconvolution algorithm and the intensity ratio of the Raman characteristic peaks. The study of the viscosity properties of mold flux materials will be further analyzed and correlated employing the deconvolution algorithm approach.

Based on previous studies of mold fluxes, Raman spectra often contain some overlapping peaks [9], [12]. Deconvolution analysis of the Raman spectra is necessary to achieve a qualitative and quantitative description of different structural units. It is assumed that the Raman peak follows a Gaussian function and is fitted only in regions where prominent shoulders or peaks are observed or rigorously demonstrated by previous studies [9], [12], [36]. The Raman spectra, after deconvolution analysis, can reflect all possible structures represented by peaks located at different positions. Furthermore, it is considered that silicates play a crucial role in the degree of polymerization of the melt since the content of SiO$_2$ is high relative to other components in the molten flux samples. The mole fraction of silica was further obtained by deconvolution of the Raman spectrum. Deconvolution results of the Raman spectra by Gaussian fitting are shown in Fig. 6.
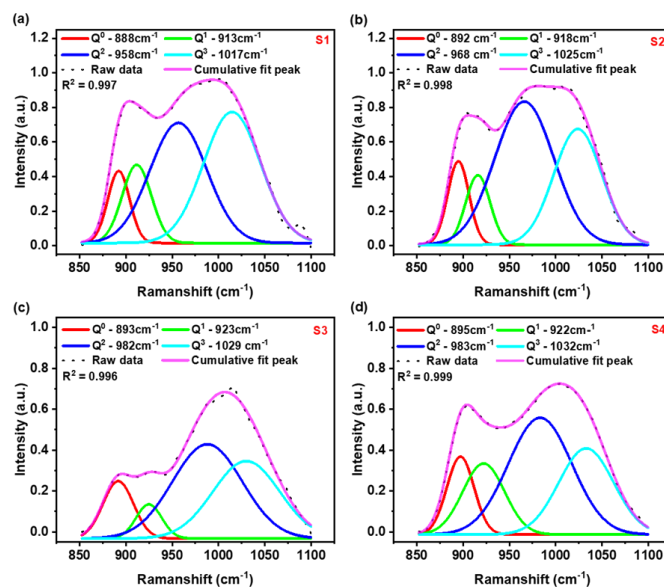


Fig. 6. Deconvoluted Raman spectra of 1400 °C synthetic fluxes for the Q region from 850-1100 cm$^{-1}$ for sample 1 to sample 4. Four individual peaks were identified from all four samples. The cumulative fit peak (pink) has been compared with the raw data and provides the R square value to address the uncertainties.

In the 850-1100 cm$^{-1}$ Raman shift region, the Qi (Si) stretching band was deconvoluted into four typical peaks. They are located at 850-895 cm$^{-1}$ (Q$^0$), 905-925 cm$^{-1}$ (Q$^1$), 945-985 cm$^{-1}$ (Q$^2$) and 1015-1100 cm$^{-1}$ (Q$^3$). These peaks correspond to the stretching vibrations of [SiO$_4$] Q$^0$, [Si$_2$O$_7$] Q$^1$, [SiO$_3$] Q$^2$, and [Si$_2$O$_5$] Q$^3$, respectively [9], [12], [36]. Details of the identified peaks are presented in Fig. 6. The sum peak fit was produced by summing the four deconvoluted Raman peaks. The R-squared value was calculated by comparing the Raw Raman data and the cumulative peak fit. An R-squared value above 99.6% addresses any uncertainties in the deconvolution process. Compared with the available literature [9], [12], it was

determined that for the flux samples at 1400 °C, the $Q^0$ (monomer) peak exhibits a slight shift to the right, and the $Q^3$ (sheet) peak exhibits a slight shift to the left. These shifts can be explained by the fact that monomer and sheet content decrease slightly at high temperatures compared to the rapidly quenched sample results presented in the previous studies [9], [12], [14], [36]. These findings also demonstrate that the flux samples at high temperatures exhibit significantly different Raman signals from the quenched flux samples for the cooling rates employed in this study. Thus, it is further demonstrated that the intrinsic physical properties of the quenched flux sample change due to the cooling process. Therefore, studying the Raman signals to understand changes in properties at high temperatures is of significant interest.

In the $CaO-Al_2O_3-SiO_2$-based mold fluxes, $SiO_2$ is the main network former as alumina is a conditional glass former (does not form a glass in the absence of other network formers). Moreover, the alumina content in these mold fluxes is low. In the silica network, four oxygen anions surround the center of each Si cation, and Si-O-Si bonds interconnect all the tetrahedral $SiO_4^{4-}$ complexes. Some Si-O-Si bonds will break when $Na^+$ or $Ca^{2+}$ ions from $Na_2O$ or CaO are present. Therefore, when the melt has a high $CaO/SiO_2$ ratio like sample 4, many network breakers in the melt are used to break the Si-O-Si bonds; however, they can also promote the formation of $[AlO_4]^{5-}$, which indicates that the Q region in the Raman spectrum is most affected by the breakage of the Si-O-Si bond when the CaO content is high. Thus, based on previous studies from JH Park, the ratio of $Q^3/Q^2$ can potentially be used as a polymerization index to quantify the effect of silicate structure on melt viscosity [37]. In addition, the $Q^0$ (monomer) has been investigated as a factor affecting the properties of mold flux materials [36], [38], [39]. Therefore, in this paper, the Raman peak intensity ratios of $Q^3/Q^2$ and $Q^3/Q^0$ after deconvolution were studied and correlated with the weight percents of CaO and $SiO_2$ and basicity. The main components of the synthetic flux samples employed in this study are $SiO_2$, CaO, and $Al_2O_3$. The content of $Al_2O_3$ was fixed at 4.69% for all four samples. Therefore, the flux structure is strongly influenced by the ratios of $CaO/Al_2O_3$ and $SiO_2/Al_2O_3$. Fig. 7 shows a scatter plot of the Q region peak intensity ratios with chemical composition and sample basicity analysis. A linear regression analyses was performed and fitted on the data points.

As shown in Fig. 7(a), the $Q^3/Q^2$ and $Q^3/Q^0$ ratios increase as the weight percent content of CaO decreases. On the other hand, as the $SiO_2$ content increases, the degree of polymerization of the silicate network increases, which corresponds to an increase in the $Q^3/Q^2$ and $Q^3/Q^0$ ratios. Finally, the $Q^3/Q^2$ and $Q^3/Q^0$ ratios correlate with the basicity of the four mold flux compositions. Both $Q^3/Q^2$ and $Q^3/Q^0$ values linearly decrease with increasing basicity, with $Q^3/Q^0$ versus basicity exhibiting a linear correlation of 99.5%. The relative peak ratios based on the Q region peaks can be seen as a well-correlated basicity indicator since substantial differences in intensity are always present. However, the peak area ratio (mole fraction) is more robust than the peak intensity and has been wildly used in previous studies [9], [12], [36]-[38].
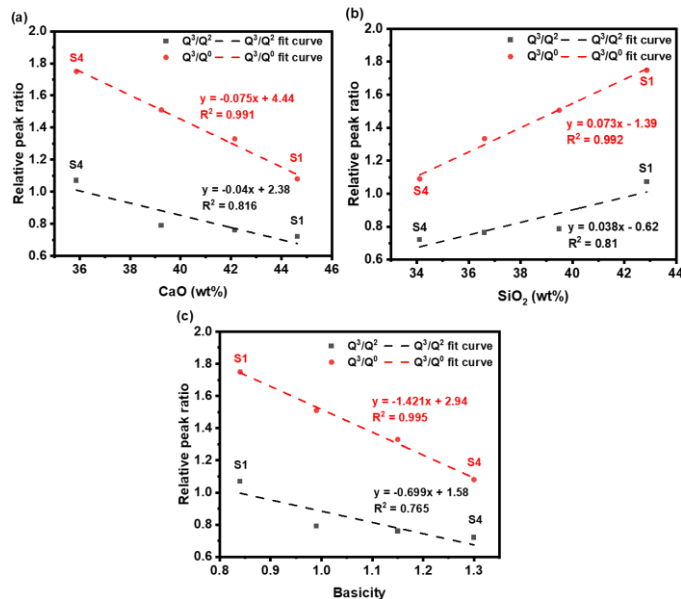


Fig. 7. Correlations of the Q region peak intensity ratio $Q^3/Q^2$ and $Q^3/Q^0$ to both flux chemical composition and basicity. (a) Q region peak intensity ratios of $Q^3/Q^2$ and $Q^3/Q^0$ versus CaO (wt%). (b) Q region peak intensity ratios of $Q^3/Q^2$ and $Q^3/Q^0$ versus $SiO_2$ (wt%). (c) Q region peak intensity ratios of $Q^3/Q^2$ and $Q^3/Q^0$ versus flux basicity.
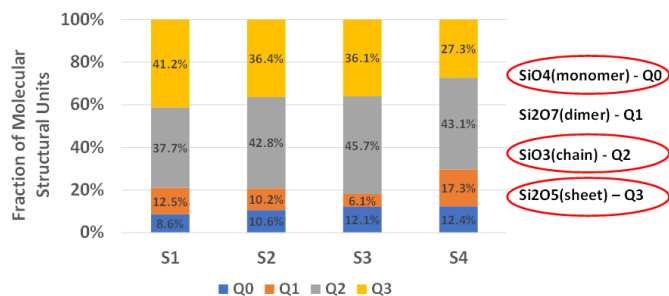


Fig. 8. Bar chart of the fraction of molecular structural units determined from deconvoluted Raman spectra of synthetic flux samples. The amount of monomer increases with the CaO (wt%) increase. The amount of sheet decreases with the $SiO_2$ (wt%) decrease. Sample 4 contains the highest amount of monomer has the highest basicity.

The combined areas of all deconvoluted peaks are a semi-quantitative estimation of the number of $Q^i$ units. Therefore, peak areas were calculated for each flux sample, as shown in Fig. 8. It reveals that the content of $Q^0$ (monomer) gradually increases, and the content of $Q^3$ (sheet) gradually decreases as the content of $SiO_2$ decreases. Sample 4, which contains the lowest amount of $SiO_2$, produces the least amount of sheet compared with the other three samples. To compare the correlation more effectively, the peak area ratios of $Q^3/Q^2$ and $Q^3/Q^0$ were also compared with the flux chemical composition, as shown in Fig. 9(a) and (b). Peak area ratios of $Q^3/Q^2$ and $Q^3/Q^0$ are positively correlated with the content of $SiO_2$. The signs of the correlations that were found are consistent with linear trends. With the increase of $SiO_2$ content, peak area ratios of $Q^3/Q^2$ and $Q^3/Q^0$ also increased, and the R-squared coefficient for the fitting was greater than 96%. Conversely, the CaO content was negatively correlated with $Q^3/Q^2$ and $Q^3/Q^0$ peak area ratios. With increasing $SiO_2$ content, peak area ratios of $Q^3/Q^2$ and $Q^3/Q^0$ decreased. Finally, peak area ratios of $Q^3/Q^2$

TABLE II. THE CHEMICAL COMPOSITION (IN %) AND PHYSICAL PROPERTIES OF INDUSTIAL FLUX SAMPLES.

| Comp. wt% | Sample A | | | Sample B | | | Sample C | | | Sample D | | | Sample E | | |
|---|---|---|---|---|---|---|---|---|---|---|---|---|---|---|---|
| | Powder | Flux | Range | Powder | Flux | Range | Powder | Flux | Range | Powder | Flux | Range | Powder | Flux | Range |
| SiO2 | 35.9 | 39.5 | `+/- 1 | 40.9 | 45.2 | `+/- 1 | 33.6 | 38 | `+/- 1 | 31.2 | 35.1 | `+/- 1 | 33.5 | 37.5 | `+/- 1 |
| Al2O3 | 5.8 | 6.6 | `+/- 0.5 | 6.3 | 7.2 | `+/- 0.5 | 5.3 | 6.3 | `+/- 0.5 | 4 | 4.7 | `+/- 0.5 | 4.7 | 5.4 | `+/- 0.5 |
| CaO | 39.4 | 43.6 | `+/- 1 | 35.4 | 39.2 | `+/- 1 | 30.5 | 34.5 | `+/- 1 | 40.2 | 45.2 | `+/- 1 | 33 | 36.7 | `+/- 1 |
| MgO | 0.9 | 1.2 | `+/- 0.5 | 0.8 | 1 | `+/- 0.5 | 2.3 | 2.5 | `+/- 0.5 | 1.7 | 2.1 | `+/- 0.5 | 1.4 | 1.6 | `+/- 0.5 |
| Na2O | 3.5 | 4.4 | `+/- 0.6 | 3 | 3.8 | `+/- 0.6 | 10.2 | 10.3 | `+/- 0.6 | 6.3 | 7.2 | `+/- 0.6 | 10.6 | 11.3 | `+/- 0.6 |
| Fe2O3 | 0.7 | 0.9 | | 0.5 | 0.6 | | 0.5 | 0.4 | | 0.5 | 0.6 | | 0.34 | 0.7 | |
| Floride | 6.5 | 6.9 | | 5.3 | 5.6 | | 8 | 8.7 | | 8.3 | 8.9 | | 8.4 | 9 | |
| Li2O | 0.05 | 0.5 | | 1 | 1.1 | | 1.2 | 1.4 | | 0.4 | 0.4 | | 0.4 | 0.4 | |
| CaO/SiO2 | 1.1 | 1.097 | `+/- 0.03 | 0.87 | 0.866 | `+/- 0.03 | 0.91 | 0.908 | `+/- 0.03 | 1.29 | 1.288 | `+/- 0.03 | 0.98 | 0.985 | `+/- 0.03 |
| Visc. 1300C | 2.8 | | | 6.6 | | | 1.5 | | | 1 | | | 1.5 | | |
| Free carbon | 3.7 | | | 2.3 | | | 2.9 | | | 2.9 | | | 2.8 | | |
| Total carbon | 5.5 | | | 4.4 | | | 4.8 | | | 4.9 | | | 4.1 | | |
| Moisture | 0.5 max | | | 0.5 | | | 0.5 max | | | 0.5 max | | | 0.5 max | | |

and $Q^3/Q^0$ were compared with the sample basicity values, as shown in Fig. 9(c). The peak area ratios of $Q^3/Q^2$ and $Q^3/Q^0$ were negatively correlated with sample basicity with high R-squared values of 94% and 95%, respectively. The data trend indicates that both peak intensity ratio and area ratio show promising correlations with the flux sample composition and properties. Previous researchers have noted that the $Q^3/Q^2$ area ratio can be employed to estimate flux viscosity [37], which agrees with this study's result. In addition, it was also determined that the $Q^3/Q^0$ area ratio could be considered an essential parameter for the correlation of mold flux properties to parameters extracted from the measured Raman spectra. A linear relationship based on the data can be used in the steelmaking process to guide changes in flux composition in real time—to an approximate degree. It is beneficial to guide on fixing fluxes: (1) use the sign of the slope to specify the addition of a chemical; (2) use the magnitude of the slope to specify how many chemicals to add.
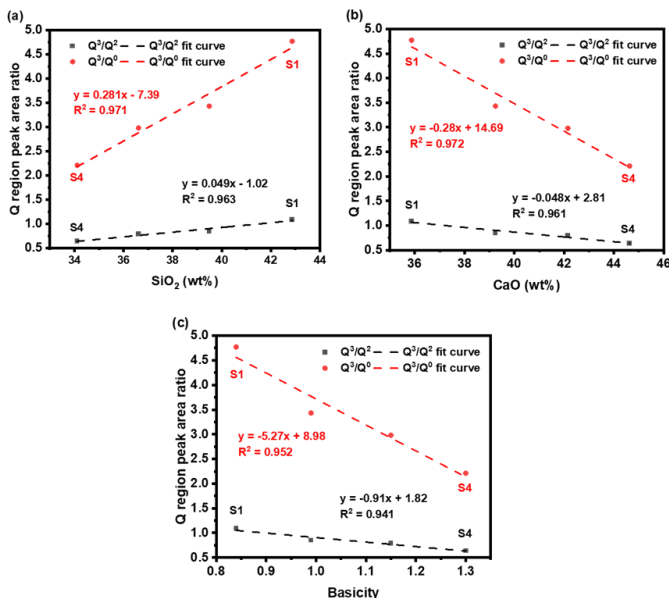


Fig. 9. Correlations obtained from Q region peak area ratios $Q^3/Q^2$ and $Q^3/Q^0$ with the flux chemical composition and basicity. (a) Q region peak area ratios

of $Q^3/Q^2$ and $Q^3/Q^0$ versus $SiO_2$ (wt%). (b) Q region peak area ratios of $Q^3/Q^2$ and $Q^3/Q^0$ versus CaO (wt%). (c) Q region peak area ratios of $Q^3/Q^2$ and Q3/Q0 versus flux basicity.

*B. High-temperature Raman Spectroscopic Analysis of Industrial Flux Samples*

After observing the relationships between parameters extracted from Raman spectra and the chemical composition of synthetic fluxes, *in situ* fiber-optic Raman spectroscopy analysis was also employed on more complex commercial flux samples provided by an industrial partner in the study. Five samples with different chemical compositions, as shown in Table II, were tested. According to the previous analysis, the Si-O-Si stretching band peak intensities and areas directly correlate to the magnitudes of the molten flux basicity. Therefore, flux samples with reported viscosity values of 2.8, 6.6, 1.5, 1, and 1.5 at 1300 °C were examined using high-temperature Raman spectroscopy.

To clearly understand the Q region Raman spectra of the industrial flux sample under different temperature conditions, real-time Raman spectra were collected for Sample A from room temperature to 1350 °C, and the results are included in Fig.10. As can be observed, these Raman spectra showed remarkable spectral variations with temperature. The Raman spectral range between 475 cm$^{-1}$ and 1125 cm$^{-1}$ is composed of two significant regions for this study, i.e., 500-700 cm$^{-1}$ and 800-1100 cm$^{-1}$.

In the Raman spectral region of 500-700 cm$^{-1}$, a peak at 540 cm$^{-1}$ and a peak at 645 cm$^{-1}$ correspond with the stretch vibration of Al-O-Al and the bending vibration of Si-O-Si [1], [5], [9], [12], [14], [33], [35], [36]. The alumina peak in the industrial flux sample appears to be slightly shifted from 525 to 540 cm$^{-1}$ compared to the synthetic flux samples shown in Fig. 3. This observation indicates that the higher $CaO/SiO_2$ ratio, which causes more network breakages (non-bridging oxygens) in the Si-O-Si bonds and concomitantly promotes the formation of $[AlO_4]^{5-}$. Raman spectra of the alumina and silica region (500-700 cm$^{-1}$) are invariant at high temperatures. The most significant spectral changes with temperature increases are observed in the Q region (800-1100 cm$^{-1}$). The first obvious spectral change occurred between room temperature and 800

°C, where the sample was fully solid and contained crystallites. Between 800 and 1000 °C, the flux sample was still solid but above the crystallization initiation temperature, with no significant changes observed in the Q region. In the range between 1200 °C and the flux melting point temperature, the Q region appeared to have a second significant change due to Si-O stretching bond breaking. At 1350 °C, with the sample entirely in the liquid phase, the Raman spectra exhibited additional changes in the Q region that appear directly affected by the increase in temperature. Monitoring these changes with temperature may prove to be a promising method for tracking the viscosity-temperature dependence of industrial flux samples.
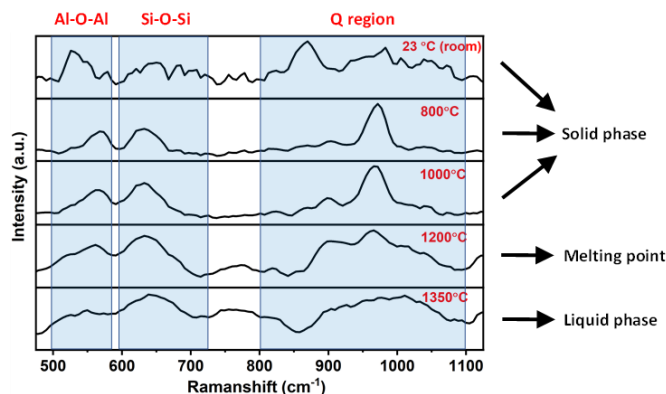


Fig. 10. Raman spectra recorded from the industrial sample A at different temperature conditions. Three highlighted regions were identified as alumina and silica from 500-700 cm$^{-1}$ and Q region from 800-1100 cm$^{-1}$. Q region Raman spectra significantly changed along with the temperature increase.
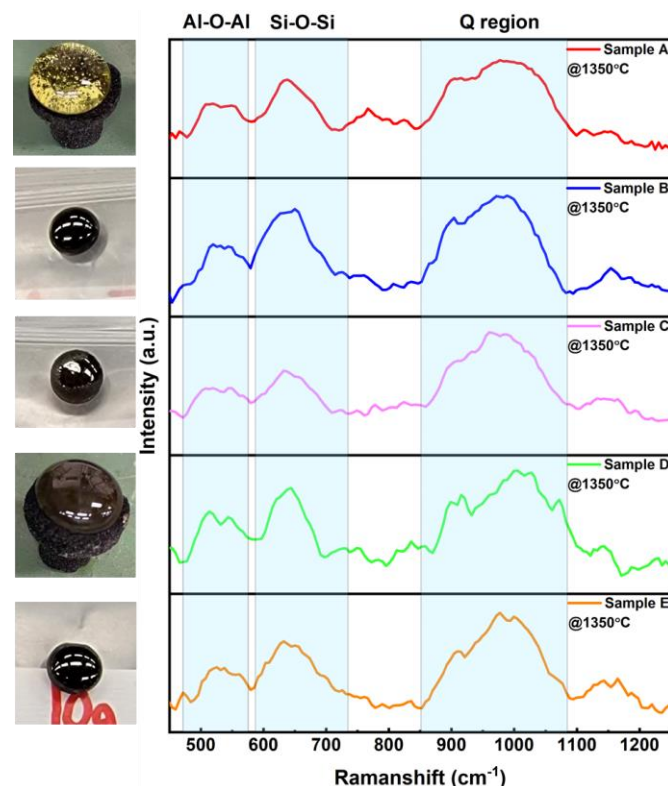


Fig. 11. Images of the industrial mold flux samples after the quenching process (left). Raman spectra recorded from five industrial flux samples at 1350 °C (right). Alumina, silica, and Q region Raman spectra were identified. The Q region Raman spectra changed with different flux chemical compositions.

High-temperature Raman spectra of five industrial flux samples were successfully collected at 1350 °C, as shown in Fig. 11. Images of the mold flux samples after quenching are shown on the left side of Fig. 11. The color of these quenched samples varied with composition. Although all five spectra exhibited significant Raman peaks in the Al-O-Al bond region, the bending vibration of Si-O-Si, and the Q region (Qi), which matches the previous results from the synthetic flux samples. Since samples D and E contain very similar viscosity values to sample C, the three industrial flux samples A through C, were selected to study the relationship between Raman spectra and chemical composition; the results are shown in Fig. 12. Four individual Q$^i$ peaks were deconvoluted from the original Raman spectra. A greater than 99.4% R-squared value indicates the matching coefficient of cumulative fit for the deconvolution process, providing additional confidence in our approach.

According to the deconvolution result shown in Fig. 12, the Q region Raman spectra have no significant shift compared with the result from the synthetic flux sample as shown in Fig. 6. Based on the study of synthetic flux samples detailed in the previous section, the Raman peak intensity ratios of Q$^3$/Q$^2$ and Q$^3$/Q$^0$ were calculated to study the correlation between the Raman spectrum and viscosity. As shown in Fig. 13, the fitted curves for both the Q$^3$/Q$^2$ and Q$^3$/Q$^0$ versus viscosity plots associated with the industrial flux samples show a negative linear correlation. It is noteworthy that the Raman peak intensity ratio of Q$^3$/Q$^2$ versus viscosity revealed an R-squared value of 97.1%.
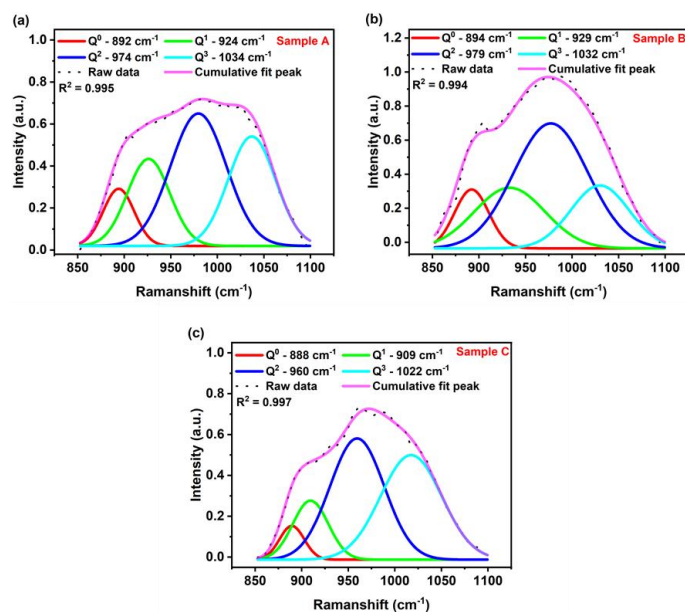


Fig. 12. Deconvoluted Raman spectra of 1350 °C industrial flux samples for the Q region from 850-1100 cm$^{-1}$ for sample A to sample C. Four individual peaks were identified from all four samples. The cumulative fit peak (pink) has been compared with the raw data and provides the R square value to address the uncertainties.

Based on the data analysis results for the synthetic flux samples detailed in the previous section, the area fraction of each individual Raman peak in the Q region was calculated and is shown in Fig. 14. It can be seen from the graphs that the mole fraction of Q$^0$ (monomer) and Q$^1$ (dimer) decreases, and Q$^3$ (sheet) increases as the viscosity of the industrial flux sample

decreases. Sample B, which has the highest viscosity and lowest basicity contains the most amount of $Q^0$. This conclusion is also consistent with the previous findings for the synthetic flux samples. Finally, the area ratios of $Q^3/Q^2$ and $Q^3/Q^0$ were compared with the viscosity of the industrial flux samples, as shown in Fig. 15. It was found that the curve trends of $Q^3/Q^2$ and $Q^3/Q^0$ are negatively correlated with the viscosities of the industrial flux samples. A linear regression analyses was performed and fitted on the data points. The accuracy of the linear correlation for both parameters was above 92%.
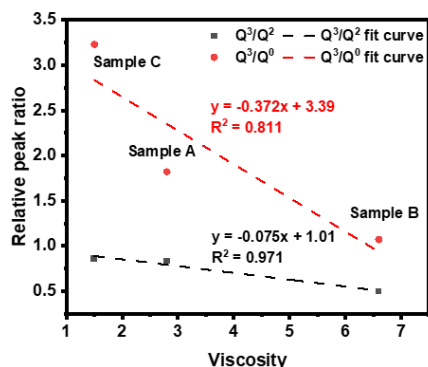


Fig. 13. Correlations obtained from Q region peak intensity ratios $Q^3/Q^2$ and $Q^3/Q^0$ with the industrial flux sample viscosity. A negative correlation was found for both peak intensity ratios.
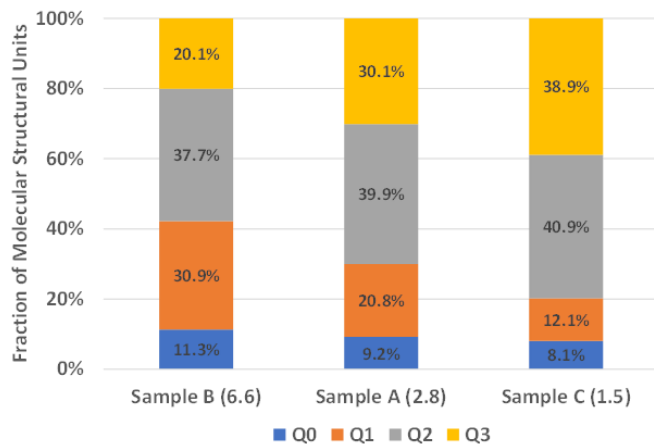


Fig. 14. Bar chart of the fraction of molecular structural units determined from deconvoluted Raman spectra of the industrial flux samples. The viscosity value of each samples displays in the bracket. Sample B, which has the highest viscosity and lowest basicity contains the most amount of $Q^0$.
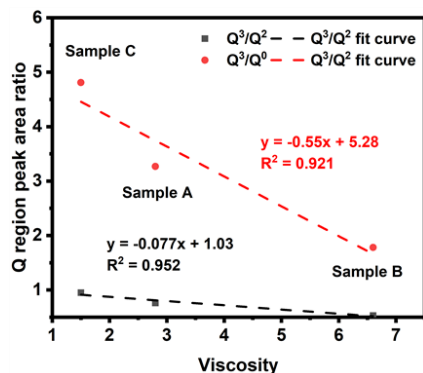


Fig. 15. Q region peak area ratios $Q^3/Q^2$ and $Q^3/Q^0$ with the industrial flux sample viscosity. A negative correlation was found for both peak area ratios.

## IV. CONCLUSION

This paper reports, for the first time, an alternative method for real-time mold flux analysis using an *in situ* fiber-optic Raman sensor that can be used directly in a 1400 °C high-temperature environment. Raman spectroscopy uniquely identifies specific molecules through high-resolution metering of vibrational bands, providing insights into the molecular structures in materials. In this work, direct online processing of molten flux samples to determine the chemical composition, basicity, and viscosity appears feasible. The work shows the advantages of using a fiber-optic probe for conducting Raman spectroscopy at high temperatures to assess chemical structures and compositions in mold flux. Furthermore, results from Raman spectroscopy show that a range of chemistries can be successfully captured using an *in situ* fiber-optic Raman sensor at 1400 °C. Experimental results also show the difference between the Raman spectra of mold fluxes in the high-temperature molten state and the previously reported Raman spectra of rapidly quenched mold fluxes at room temperature. By deconvoluting the high-temperature Raman spectra, it was determined that both the $Q^3/Q^2$ ratio (sheet/chain) and the $Q^3/Q^0$ (sheet/monomer) ratio could be used to assess the chemical composition and physical properties of the mold flux. Furthermore, a relationship between Raman peak ratios versus the sample basicity, viscosity, and chemical composition of the mold flux samples was also identified, which shows promise for online flux analysis. In addition, the proposed *in situ* and real-time high-temperature Raman sensor can be employed for studying slags, bio-organic glass, crystalline materials, and cement-based materials at high temperatures for material science, biochemical, civil engineering, and other applications.

## ACKNOWLEDGEMENT

## REFERENCES

[1] J. Gao, G. Wen, T. Huang, and P. Tang, "The structure and the crystallization behaviour of the Cao-SiO2-Al2O3-based mold flux for high-al steels casting," *Advances in Molten Slags, Fluxes, and Salts: Proceedings of the 10th International Conference on Molten Slags*, Fluxes and Salts 2016, pp. 291–298, 2016.

[2] S. Turteltaub and A. Suiker, "Transformation-induced plasticity in ferrous alloys," *Journal of the Mechanics and Physics of Solids*, vol. 53, no. 8, pp. 1747–1788, 2005.

[3] J. Li, B. Kong, L. Jiang, D. Jia, S. Ren, J. Yang, Q. Liu, Q. Shu, and K. Chou, "Effect of B2O3 on slag-metal reaction between Cao-Al2O3-based mold flux and High Aluminum Steel," *High Temperature Materials and Processes*, vol. 37, no. 9-10, pp. 981–985, 2018.

[4] J. Yang, H. Cui, J. Zhang, O. Ostrovski, C. Zhang, and D. Cai, "Interfacial reaction between high-al steel and Cao-Al2O3-based mold fluxes with different CaO/Al2O3 ratios at 1773 K (1500 °C)," *Metallurgical and Materials Transactions B*, vol. 50, no. 6, pp. 2636–2646, 2019.

[5] G.-H. Kim and I. Sohn, "Effect of al2o3 on the viscosity and structure of calcium silicate-based melts containing Na2O and CaF2," *Journal of Non-Crystalline Solids*, vol. 358, no. 12-13, pp. 1530–1537, 2012.

[6] B. Lu, K. Chen, W. Wang, and B. Jiang, "Effects of Li2O and Na2O on the crystallization behavior of lime-alumina-based mold flux for casting high-al steels," *Metallurgical and Materials Transactions B*, vol. 45, no. 4, pp. 1496–1509, 2014.

[7] J. Gao, G. Wen, Q. Sun, P. Tang, and Q. Liu, "The influence of Na2O on the solidification and crystallization behavior of CaO-SiO2-Al2O3-based Mold Flux," *Metallurgical and Materials Transactions B*, vol. 46, no. 4, pp. 1850–1859, 2015.

[8] M.-D. Seo, C.-B. Shi, J.-W. Cho, and S.-H. Kim, "Crystallization behaviors of CaO-SiO2-Al2O3-NA2O-Caf2-(Li2O-B2O3) mold fluxes," *Metallurgical and Materials Transactions B*, vol. 45, no. 5, pp. 1874–1886, 2014.

[9] W. Yan, G. Zhang, and J. Li, "Viscosity and structure evolution of CaO–SiO2-based mold fluxes with involvement of CaO–Al2O3-based Tundish fluxes," *Ceramics International*, vol. 46, no. 9, pp. 14078–14089, 2020.

[10] Z. Zhang, G. Wen, P. Tang, and S. Sridhar, "The influence of Al2O3/SiO2 ratio on the viscosity of mold fluxes," *ISIJ international*, vol. 48, no. 6, pp. 739-746, 2008.

[11] Y. He, X. Shen, Y. Jiang, and A. Lu, "Effects of li2o replacing Na2O on glass forming, structure and properties of Na2O–MgO–Al2O3–SiO2 glass and glass-ceramics," *Materials Chemistry and Physics*, vol. 258, p. 123865, 2021.

[12] J. Gao, G. Wen, T. Huang, P. Tang, and Q. Liu, "Effects of the composition on the structure and viscosity of the CaO–SiO2-based Mold Flux," *Journal of Non-Crystalline Solids*, vol. 435, pp. 33–39, 2016.

[13] G. Wen, S. Sridhar, P. Tang, X. Qi, and Y. Liu, "Development of fluoride-free mold powders for peritectic steel slab casting," *ISIJ International*, vol. 47, no. 8, pp. 1117–1125, 2007.

[14] J. Gao, G. Wen, T. Huang, B. Bai, P. Tang, and Q. Liu, "Effect of slag-steel reaction on the structure and viscosity of Cao-SiO2-based mold flux during high-al steel casting," *Journal of Non-Crystalline Solids*, vol. 452, pp. 119–124, 2016.

[15] K. C. Mills, A. B. Fox, Z. Li, and R. P. Thackray, "Performance and properties of mould fluxes," *Ironmaking & Steelmaking*, vol. 32, no. 1, pp. 26–34, 2005.

[16] J. Liao, Y. Zhang, S. Sridhar, X. Wang, and Z. Zhang, "Effect of Al2O3/SiO2 ratio on the viscosity and structure of slags," *ISIJ international*, vol. 52, no. 5, pp. 753-758, 2012.

[17] L. Zhou, W. Wang, B. Lu, G. Wen, and J. Yang, "Effect of basicity and B2O3 on viscosity, melting and crystallization behaviors of low fluorine mold fluxes for casting medium carbon steels," *Metals and Materials International*, vol. 21, no. 1, pp. 126–133, 2015.

[18] G. H. Kim and I. Sohn, "Role of B2O3 on the viscosity and structure in the cao-al2o3-NA2O-based system," *Metallurgical and Materials Transactions B*, vol. 45, no. 1, pp. 86–95, 2013.

[19] E. Brauchle and K. Schenke‐Layland, "Raman spectroscopy in biomedicine – non‐invasive in vitro analysis of cells and extracellular matrix components in tissues," *Biotechnology Journal*, vol. 8, no. 3, pp. 288–297, 2012.

[20] H. Lin, H. J. Lee, N. Tague, J.-B. Lugagne, C. Zong, F. Deng, J. Shin, L. Tian, W. Wong, M. J. Dunlop, and J.-X. Cheng, "Microsecond fingerprint stimulated Raman spectroscopic imaging by ultrafast tuning and spatial-spectral learning," *Nature Communications*, vol. 12, no. 1, 2021.

[21] J. W. Kang, Y. S. Park, H. Chang, W. Lee, S. P. Singh, W. Choi, L. H. Galindo, R. R. Dasari, S. H. Nam, J. Park, and P. T. So, "Direct observation of glucose fingerprint using in vivo Raman spectroscopy," *Science Advances*, vol. 6, no. 4, 2020.

[22] M. Y. Elsayed, A. M. Gouda, Y. Ismail, and M. A. Swillam, "Silicon-based sers substrates fabricated by electroless etching," *Journal of Lightwave Technology*, vol. 35, no. 14, pp. 3075–3081, 2017.

[23] T. Mi, Y. Li, W. Liu, W. Li, W. Long, Z. Dong, Q. Gong, F. Xing, and Y. Wang, "Quantitative evaluation of cement paste carbonation using Raman spectroscopy," *npj Materials Degradation*, vol. 5, no. 1, 2021.

[24] Y. Yue, J. J. Wang, P. A. M. Basheer, and Y. Bai, "In-situ monitoring of early hydration of clinker and Portland cement with optical fiber excitation Raman spectroscopy," *Cement and Concrete Composites*, vol. 112, p. 103664, 2020.

[25] Y. Gao, N. Yang, S. Lu, T. You, and P. Yin, "in situ monitoring of plasmon-driven photocatalytic reactions at gas–liquid–solid three-phase interfaces by surface-enhanced Raman spectroscopy," *Journal of Materials Chemistry C*, vol. 7, no. 32, pp. 9926–9932, 2019.

[26] Y. Chen, H. Liu, Y. Tian, Y. Du, Y. Ma, S. Zeng, C. Gu, T. Jiang, and J. Zhou, "In situ recyclable surface-enhanced Raman scattering-based detection of multicomponent pesticide residues on fruits and vegetables by the flower-like mos2@ag hybrid substrate," *ACS Applied Materials & Interfaces*, vol. 12, no. 12, pp. 14386–14399, 2020.

[27] M. Azkune, T. Frosch, E. Arrospide, G. Aldabaldetreku, I. Bikandi, J. Zubia, J. Popp, and T. Frosch, "Liquid-core microstructured polymer optical fiber as fiber-enhanced Raman spectroscopy probe for glucose sensing," *Journal of Lightwave Technology*, vol. 37, no. 13, pp. 2981–2988, 2019.

[28] B. Zhang, R. E. Gerald, and J. Huang, "Miniaturized 7-in-1 fiber-optic Raman probe," *Optics Letters*, vol. 47, no. 21, p. 5561, 2022.

[29] X. Li, Y. Zhang, B. Xue, X. Kong, X. Liu, L. Tu, Y. Chang, and H. Zhang, "A SERS nano-tag-based fiber-optic strategy for in situ immunoassay in unprocessed whole blood," *Biosensors and Bioelectronics*, vol. 92, pp. 517–522, 2017.

[30] C. Krafft, S. Dochow, I. Latka, B. Dietzek, and J. Popp, "Diagnosis and screening of cancer tissues by fiber-optic probe Raman spectroscopy," *Biomedical Spectroscopy and Imaging*, vol. 1, no. 1, pp. 39–55, 2012.

[31] P. F. McMillan, B. T. Poe, P. H. Gillet, and B. Reynard, "A study of SiO2 glass and supercooled liquid to 1950 K via high-temperature Raman spectroscopy," *Geochimica et Cosmochimica Acta*, vol. 58, no. 17, pp. 3653–3664, 1994.

[32] W. J. Malfait and W. E. Halter, "Structural relaxation in silicate glasses and melts: High-temperature Raman spectroscopy," *Physical Review B*, vol. 77, no. 1, 2008.

[33] I. Daniel, P. Gillet, B. T. Poe, and P. F. McMillan, "In-situ high-temperature Raman spectroscopic studies of aluminosilicate liquids," *Physics and Chemistry of Minerals*, vol. 22, no. 2, 1995.

[34] D. R. Neuville, L. Cormier, and D. Massiot, "Al environment in tectosilicate and Peraluminous Glasses: A 27al MQ-Mas NMR, Raman, and xanes investigation," *Geochimica et Cosmochimica Acta*, vol. 68, no. 24, pp. 5071–5079, 2004.

[35] Y. Tsunawaki, N. Iwamoto, T. Hattori, and A. Mitsuishi, "Analysis of CaO-SiO2 and CaO-SiO2-CaF2 glasses by Raman spectroscopy," *Journal of Non-Crystalline Solids*, vol. 44, no. 2-3, pp. 369–378, 1981.

[36] W. Wang, S. Dai, L. Zhou, J. Zhang, W. Tian, and J. Xu, "Viscosity and structure of mgo–sio2-based slag melt with varying B2O3 content," *Ceramics International*, vol. 46, no. 3, pp. 3631–3636, 2020.

[37] J. H. Park, "Composition–structure–property relationships of CaO–Mo–SiO2 (M=mg2+, MN2+) systems derived from micro-raman spectroscopy," *Journal of Non-Crystalline Solids*, vol. 358, no. 23, pp. 3096–3102, 2012.

[38] Y. Sun, Z. Zhang, L. Liu, and X. Wang, "FTIR, Raman and NMR investigation of CaO–SiO2–P2O5 and CaO–SiO2–TiO2–P2O5 glasses," *Journal of Non-Crystalline Solids*, vol. 420, pp. 26–33, 2015.

[39] Y. U. Han and D. J. Min, "The cationic effect on properties and structure of CaO-MgO-SiO2 Melts," *Advances in Molten Slags, Fluxes, and Salts*, pp. 501–509, 2016.

[40] L. Zhang, W. Wang, S. Xie, K. Zhang, and I. Sohn, "Effect of basicity and B2O3 on the viscosity and structure of fluorine-free mold flux," *Journal of Non-Crystalline Solids*, vol. 460, pp. 113–118, 2017.